Effectiveness of Specularity Removal from Hyperspectral Images on the Quality of Spectral Signatures of Food Products

Gamal ElMasry [1,2] Pere Gou [1] Salim Al-Rejaie[3]

[1] *Institute of Agriculture and Food Research and Technology (IRTA), Finca Camps i Armet s/n, 17121, Monells, Spain (Tel. +34 666293308, Fax: +34 972630980, Email: gamal.masry@irta.cat)*

[2] *Suez Canal University, Faculty of Agriculture, Agricultural Engineering Department, Ismailia, Egypt*

[3] *Department of Pharmacology & Toxicology, College of Pharmacy, King Saud University, Riyadh 11564, Saudi Arabia*

Abstract

Specularity or highlight problem exists widely in hyperspectral images, provokes reflectance deviation from its true value, and can hide major defects in food objects or detecting spurious false defects causing failure of inspection and detection processes. In this study, a new non-iterative method based on the dichromatic reflection model and principle component analysis (PCA) was proposed to detect and remove specular highlight components from hyperspectral images acquired by various imaging modes and under different configurations for numerous agro-food products. To demonstrate the effectiveness of this approach, the details of the proposed method were described and the experimental results on various spectral images were presented. The results revealed that the method worked well on all hyperspectral and multispectral images examined in this study, effectively reduced the specularity and significantly improves the quality of the extracted spectral data. Besides the spectral images from available databases, the robustness of this approach was further validated with real captured hyperspectral images of different food materials. By using qualitative and quantitative evaluation based on running time and peak signal to noise ratio (PSNR), the experimental results showed that the proposed method outperforms other specularity removal methods over the datasets of hyperspectral and multispectral images.

Keyword: hyperspectral imaging, multispectral imaging, specularity, highlights, spectral analysis

1. Introduction

Acquisition of good hyperspectral images is very crucial for accurate detection, classification and quality prediction of essential food quality traits during food processing practices (ElMasry and Nakauchi 2016) because poor image quality negatively affects many subsequent data processing and treatments. One of the challenging tasks in processing multi-dimensional hyperspectral images with

high spectral and spatial resolutions is to extract useful information from the vast amount of data volume of numerous spectral bands (ElMasry et al., 2007). The process of extracting information from hyperspectral images, and its transformation into a useful representation, enables the description of intrinsic characteristics of objects in the scene (Khan, Thomas et al. 2017). However, the raw hyperspectral images acquired even by a fully calibrated hyperspectral imaging system may have different sorts of problems, and therefore it is not likely to produce ideal representation of the objects being imaged. That is why careful consideration of image pre-processing routines is substantially important (Achata et al., 2019). In general, all of pre-processing routines have already been described and employed by many authors for different applications (ElMasry and Nakauchi 2016; Nguyen-Do-Trong et al., 2019), but very few studies (*e.g.* Fu, Tan et al. 2006; Koirala, Pant et al. 2011; Zheng, Sato et al. 2015) were devoted towards dealing with specular problems encountered in hyperspectral images, especially those ones that will be used for real-time applications in food processing plants. In fact, the implementation of hyperspectral imaging systems at the industrial level is not straightforward, as several issues must be addressed such as noise reduction and removal of specularity highlight problems (Sivertsen, 2011). Solving specularity highlight problem of hyperspectral images in on-line food applications is very crucial and many efforts have been carried out to reach fully automated quality evaluation systems (Martin, 2007). However, a few examples have been reported in the literature for real-time applications such as those implemented for the analysis of fat content in meat trimmings, screening of fatty acid composition in intramuscular fat, and contamination and disease detection in poultry (Wold et al., 2011; Chao et al., 2008; Park et al., 2002). By overcoming some of the limitations of this technology, it is expected that hyperspectral imaging techniques will be moving from laboratories to practical real-time applications in modern food industrial control and inspection systems.

When a bundle of light rays hits a food sample, two types of reflections namely specular and diffuse reflections are generated (Shen, Zhang et al. 2008; Tan and Ikeuchi 2008; Yang, Tang et al. 2016; Guo, Zhou et al. 2018). Specular reflection is a mirror-like reflection of light from a sample causing the problem of specularity or highlights (Tan and Ikeuchi 2008; Yang, Tang et al. 2015). While the diffuse reflection depends only on the illumination direction in term of its intensity magnitude, the location of specular reflection depends on viewing and illumination directions, causing its appearance to be inconsistent (Tan, Nishino et al. 2004). Thus, to properly acquire the diffuse only reflection, a method to separate the two components robustly and accurately is required (Akashi and Okatani 2016; Guo, Zhou et al. 2018). In computer vision and hyperspectral imaging applications, the specularity problem may be ignored completely, treated as outliers, reduced or removed, or alternatively used it as a source of information (Tan and Ikeuchi 2008; Hamid 2013). The simplest way to avoid specularity problem and its influences is by using cross setting of a polarizing filter in front of the camera sensor and light source during image acquisition (Nayar, Fang et al. 1997; Yoon, Choi et al.

2006; Koirala, Pant et al. 2011; Yang, Tang et al. 2016; Nguyen-Do-Trong et al., 2019). Alternatively, it could be solved by using a low-pass filter to the maximum fraction of the chromaticity to smooth out the variance due to specular pixels in the image.

1.1. Specularity problem in RGB colour images

In all imaging modalities, it is very important to differentiate between pixels having specular highlights and saturated pixels. Pixels whose intensity values are greater than the dynamic range assigned for each pixel to record the maximum irradiance in the scene are known as saturated pixels that contain less information about the scene. Contrary to the specular pixels that are related to physics of illuminant, the scene geometry and the properties of material not due to the image sensors, saturated pixels is caused by underlying physical characteristics of the sensor which limit the highest irradiance that can be measured for the given settings of the camera. Because saturated pixels do not have unique corresponding irradiance values, they are often treated as missing values or interpolating them from surrounding pixels. Alternatively, the saturated pixels could be by certain offset correction or by applying high dynamic range imaging (Kavusi & ElGamal, 2004). Numerous experimental studies have been performed to obtain insights into specularity phenomenon and to develop models that explain the mechanisms of separating diffuse and specular components (Lehmann and Palm 2001; Tan and Ikeuchi 2008; Artusi, Banterle et al. 2011; Yamamoto, Kitajima et al. 2017). In colour images, detection of specular and diffuse pixels has been investigated intensively (Shen, Zhang et al. 2008; Shen and Zheng 2013; Nguyen, Vo et al. 2014; Suo, An et al. 2016; Yang, Tang et al. 2016) by using either single image techniques or multiple images-based techniques. In the single-image techniques, the specularity problem is detected or removed based either on colour space transformation or on spatial information analysis (Shen and Zheng 2013; Akashi and Okatani 2016; Yamamoto, Kitajima et al. 2017; Guo, Zhou et al. 2018). The second line of work for removing specularity was focused on using multiple images-based techniques that depend on acquiring a number of images at different imaging conditions. The methods of this category are less practical because multiple images with certain conditions are not always available in practice.

1.2. Specularity problem in hyperspectral images

The quality of the acquired hyperspectral images, the way of extracting spectral fingerprints and methods of data modelling have substantial effects on the outcomes of the subsequent analyses and processing. Because this kind of images is acquired at numerous contiguous wavelengths within different regions of the electromagnetic spectrum, the spectral images come also with the problem of specular highlights (Koirala, Pant et al. 2011; Khan, Thomas et al. 2017; Washburn et al., 2017). This is as true for hyperspectral images as for the conventional colour images, because specularity is most related to the physics of illuminant, the scene geometry and the properties of material not due to the image sensors used (Fu, Tan et al. 2006).

When a hyperspectral image was acquired for a highly 'homogeneous' object with consistent physicochemical characteristics, the spectral signatures of every single pixel in the image should be identical throughout the electromagnetic spectrum. However, due to relative arrangement between the camera and the sample, object geometry, illumination type and structure and the viewing angel, the specular problem may appear with different severity in the image. For instance, Figure 1a shows a pseudo-colour image rendered from a hyperspectral image acquired in the spectral range of 400-1000 nm for a homogeneous fat layer of consistent fat content along the sample. It is quite obvious to notice that this image suffers from specularity problem in the left hand side of the sample. The intensities of reflected light appeared in this spot are strong highlight and are much higher than the target intensities under or on the reflection surface, making distinguish of the effective information from the reflected highlight very difficult. Due to homogeneous fat content in the whole sample, the spectral signatures of three different points (D_1, D_2 and D_3) exactly adjacent to the specular region were quite identical despite their relative spatial locations in the image as noticeably shown in Figure 1b. Such points exhibited their intrinsic properties due to their diffuse reflectance resulting from the interaction of light rays with the sample. However, the spectral signatures of pixels inside the specular zone exactly adjacent to these three points are substantially different due to the presence of specular reflectance besides the diffuse reflectance within this zone. The spectra of two different points (S_1 and S_2) inside this zone are shown in Figure 1b demonstrating that the specular problem leads to higher reflectance values despite the homogeneity of the food sample. Although all absorption bands throughout the spectrum were all well preserved in the specular spectra, the presence of specularity amplified the reflectance magnitudes at all wavebands. Therefore, for obtaining better reliable data from hyperspectral images, it is necessary to have the image without specularity highlights (Shen and Zheng 2013; Zheng, Sato et al. 2015); otherwise, the desired objects may be obscured by highlights or detected as different objects (Koirala, Pant et al. 2011; An, Suo et al. 2015; Akashi and Okatani 2016).

Despite the negative effects of specularity problem on the magnitude of spectral data extracted from hyperspectral images, most of research in hyperspectral imaging applications for food materials was conducted under the assumption of perfect diffuse reflection without considering the specular problem or by excluding specular pixels from calculations as noise or outliers (ElMasry, Sun et al. 2013; Suktanarak, S., & Teerachaichayut, 2017). However, this may lead to unbalanced results if the size of the highlight region is very large, because the large number of pixels involved cannot be considered as outliers (Yang, Tang et al. 2015). The assumption of ignoring specularity (where it clearly exists) introduces constraints and reduces the robustness of the developed models (Khan, Thomas et al. 2017). Thus, any algorithms used directly on hyperspectral images that show high specularity can lead to misleading outcomes such as false segmentations, deceptive object measurements and recognition errors. Although, specularity is a phenomenon in spectral images acquired under reflectance mode,

very few research endeavours have been directed towards this problem in multispectral and hyperspectral images. For instance, (Fu, Tan et al. 2006) introduced a specular invariant representation for hyperspectral images based on the dichromatic model and orthogonal subspace projection (OSP) using a very simple algorithm that only involves pixel level operations without any further post-processing operations. The only assumption they made is that illumination spectra are known as a priori. (Bochko and Parkkinen 2005) exploited a mixture model of probabilistic principle component analysis (PPCA) approach to detect the highlight-affected parts and the diffuse parts from spectral images without the need of information of the light source. By developing a novel low-rank matrix factorization perspective, (Zheng, Sato et al. 2015) suggested a method based on singular value decomposition (SVD) to separate the illumination (specular) and diffuse reflectance under general spectral illumination with reasonable results in synthetic and real hyperspectral data. Also, (Koirala, Pant et al. 2011) proposed a linear positive constrained spectral un-mixing method to separate the spectral image into its highlight and diffuse components at each pixel position by assuming that the highlight-affected part is the spectral power distribution (SPD) of the light source and the other endmembers are assumed to be the spectra of pure diffuse pixels.

For practical applications of spectral imaging fields in food quality inspection operations, the ill-posed problem of specularity highlights should be mitigated and removed from all bands of the images because it conceals the real spectral properties of the examined food items, provides fake spatial and spectral information and obscures and fades the extracted data leading to misbehaving models. As the reflectance in specular highlight regions is the sum of diffuse and specular reflection components, the challenge is to separate both components from each other and keep only the diffuse reflectance that carries useful information about the sample. In practice, the other ready-to-use spectral pre-treatment routines such as standard normal variate (SNV), multiplicative scatter correction (MSC), mean centring and derivatives are unable to provide images free from specularity problem. Therefore, employing an innovative method to exclude such artefacts from the hyperspectral and multispectral images is substantially important. Therefore, the main aim of this study was to develop a new non-iterative algorithm based on the fundamentals of dichromatic reflection model and principle component analysis (PCA) to detect and remove specular highlight components from hyperspectral and multispectral images acquired by various imaging modalities and under different configurations for numerous agro-food products.

2. Methodology

2.1. Image data

To verify the robustness of the developed method of specular treatment, an extensive evaluation using various real hyperspectral images from different sources was conducted. The procedure of specular treatment used in this study was tested on different spectral images either from our previous studies

(ElMasry et al., 2012) or collected from hyperspectral and multispectral image database publicly available in the internet (*e.g.* http://www.cs.columbia.edu/CAVE/databases/multispectral). The tested spectral images were acquired in different regions of the electromagnetic spectrum from the visible (VIS), shortwave near infrared (SW-NIR) to the near infrared (NIR) regions with different spatial dimensions. Also, the images have different dynamic ranges from 12 to 14 bit and stored either in band-interleaved by pixel (bip), band-interleaved by line (bil) or band sequential (bsq) format. Spectral images of different inhomogeneous food samples were used in the experiment to evaluate the proposed method.

2.2. Dichromatic Reflection Model

A hyperspectral signal records the spectral radiance of a reflective surface, which is composed of the illumination spectral power distribution and the surface reflectance spectra (Zheng, Sato et al. 2015). Thus, in hyperspectral images of inhomogeneous objects such as food samples, the reflectance spectrum at any pixel in the image is a linear sum of diffuse and specular reflections (Koirala, Pant et al. 2011; Shen and Zheng 2013; Guo, Zhou et al. 2018). The highlight or specular component is usually due to the contribution of the spectral power distribution (SPD) of the light source. According to the dichromatic model, the reflection (I) of an inhomogeneous object (*e.g.* a piece of food sample) in the scene is a linear combination of the diffuse (I_D) and specular (I_S) components as explained in the following equation:

$$I = \alpha I_D + \beta I_S + e \qquad (1)$$

To solve the equation for each pixel, it is assumed that the illumination is stable, the specular pixels are not saturated, and the spectral camera behaves in a linear manner, which means that the sensor response values are proportional to the intensity of the light entering the sensor. As a result, the dichromatic model applied for a hyperspectral image with Ω contiguous narrow bands centred at λ_1, λ_2....., λ_Ω, could be used to calculate the reflectance spectrum $I(x)$ or the response of the camera receptor at a geometric pixel location (x) as described in equation 2:

$$\begin{bmatrix} I_{\lambda_1}(x) \\ I_{\lambda_2}(x) \\ . \\ . \\ . \\ I_{\lambda_\Omega}(x) \end{bmatrix} = \begin{bmatrix} \int \alpha(x) R_d(x,\lambda_1) E(\lambda_1) S(\lambda_1)\, d\lambda + \int \beta(x) R_s(x,\lambda_1) E(\lambda_1) S(\lambda_1)\, d\lambda \\ \int \alpha(x) R_d(x,\lambda_2) E(\lambda_2) S(\lambda_2)\, d\lambda + \int \beta(x) R_s(x,\lambda_2) E(\lambda_2) S(\lambda_2)\, d\lambda \\ . \\ . \\ . \\ \int \alpha(x) R_d(x,\lambda_\Omega) E(\lambda_\Omega) S(\lambda_\Omega)\, d\lambda + \int \beta(x) R_s(x,\lambda_\Omega) E(\lambda_\Omega) S(\lambda_\Omega)\, d\lambda \end{bmatrix} + \begin{matrix} e_1(x) \\ e_2(x) \\ . \\ . \\ . \\ e_\Omega(x) \end{matrix} \qquad (2)$$

which can be rewritten as:

$$I(x) = \int_{\Omega} \alpha(x) R_d(x,\lambda) E(\lambda) S(\lambda)\, d\lambda + \int_{\Omega} \beta(x) R_s(x,\lambda) E(\lambda) S(\lambda)\, d\lambda + e(x) \qquad (3)$$

where $I = \{I_{\lambda_1}(x), I_{\lambda_2}(x) \ldots\ldots I_{\lambda_\Omega}(x)\}$ is the reflectance vector of image intensity at a pixel (x) having a spatial coordinates of $x = \{x, y\}$ representing its 2D location. The factor α is the shading factor for diffuse reflection, β is the weighting specular factor which accounts for interface reflection and specular geometry and e is the residual noise term. The terms $R_d(x,\lambda)$ and $R_S(x,\lambda)$ represent the diffuse and specular reflectance values at pixel position (x) and wavelength λ, E(λ) is the spectral power distribution (SPD) of the illuminant at a wavelength λ, which is independent of the geometry of the object and S(λ) is the camera sensor sensitivity at a wavelength λ. In the specular term, the specular reflectance $R_s(x,\lambda)$ is similar to the spectral power distribution of the illuminant and is independent of wavelength λ and can be denoted as $R_s(x)$ for the same image sensor. Under neutral interface reflection conditions, the noise term and camera gain could be ignored and Equation (3) is simplified to the following form:

$$I(x) = \alpha(x) \int_{\Omega} R_d(x,\lambda) E(\lambda) S(\lambda)\, d\lambda + \beta(x) R_s(x) \int_{\Omega} E(\lambda) S(\lambda)\, d\lambda \qquad (4)$$

From equation 1 and 4, the diffuse and specular terms at a pixel location x are denoted by $I_D = \int_{\Omega} R_d(x,\lambda) E(\lambda) S(\lambda)\, d\lambda$ and $I_S = R_s(x) \int_{\Omega} E(\lambda) S(\lambda)\, d\lambda$, respectively. The main goal is to separate these two components from a single radiance or reflectance at each pixel position $I(x,\lambda)$.

2.3. Detection of specular highlight areas

Specular candidate pixels in the input hyperspectral image could be discovered based on the local maxima (peaks) in the maximum image '$I_{max}(x,\lambda) = max(I_{\lambda 1}, I_{\lambda 2}, I_{\lambda 3}, \ldots\ldots I_{\Omega})$' in which the pixels with very high reflectance along all wavelengths were recorded. These local maxima are the centroids of the specular regions in the maximum image. Although all specular pixels obviously appear in the maximum image with the highest intensity values compared to the intensities of the other pixels, some pixels appeared in the maximum image are not necessarily to be specular highlight pixels because the reflectance of these pixels was compared with their corresponding pixels in the rest of all bands. Thus, to identify specular highlight pixels, the maximum image was first extracted from the original hyperspectral image and a thresholding process was applied to decompose the maximum image into two regions: R_1 with strong specularity that set to one and R_2 with weak or no specularity that set to zero. In this study, the maximum intensity in the $I_{max}(x,\lambda)$ image minus three times its standard deviation was used as a threshold T_1 for separating the strongest specular pixels in

this segmentation process. Thus, all pixels whose intensity in the $I_{max}(x,\lambda)$ image exceeds this threshold were marked as the *strongest* specular pixels.

2.4. Specular separation process

In general, the specular regions appeared in the hyperspectral image are characterized by their maximum intensity along the wavebands in the spectrum compared to the other normal (diffuse) regions. To simplify the problem, the spectral power distribution (SPD) of the illuminant was assumed to equal the specular reflectance '$I_S = max(I_{max}(x,\lambda))$'. If the image was normalized to this maximum values and then scaled from 0 to 1, the value of the specular term I_S should equal 1 for each waveband (Nguyen, Vo et al. 2014). Thus, when this specular term I_S in equation (1) is replaced by the maximum values at all wavebands '$max(I_{max}(x,\lambda))$', specular image as $I_S(x,\lambda) = \beta(x)max(I_{max}(x,\lambda))$ is formed. Moreover, when the diffuse term I_D is multiplied by the diffuse factor α to produce a separated diffuse image $I_D(x,\lambda)$, Eq. (1) becomes:

$$I(x,\lambda) = I_D(x,\lambda) + I_S(x,\lambda) \qquad (5)$$

Equation 5 implies that the original reflectance spectral image $I(x,\lambda)$ is composed of a diffuse component image $I_D(x,\lambda)$ and a specular component image $I_S(x,\lambda)$. Supposing there are two adjacent pixels having diffuse reflection components of $[I_D(x,\lambda), kI_D(x,\lambda)]$, where k is a constant, these two neighbouring pixels will have reflectance value of $[I(x,\lambda), kI(x,\lambda)]$. This means that, the ratio of the diffuse reflection components does not change. Thus, the specular component for a certain pixel (x) in the image should equal $I_S(x,\lambda) = k(x)\beta(x)max\left(I_{max}(x,\lambda)\right)$, with $k(x)$ being an adjustment scale at a pixel position (x) (Koirala, Pant et al. 2011). Then, the separated diffuse reflection component image $I_D(x,\lambda)$ of a pixel (x) at a wavelength λ is calculated as:

$$I_D(x,\lambda) = I(x,\lambda) - k(x)\beta(x)max\left(I_{max}(x,\lambda)\right) \qquad (6)$$

The scaling factor k was introduced to adjust the specularity level to obtain a smooth and natural diffuse component over the whole image at any wavelength as shown in Figure 1b. Accordingly, the brightest region in the hyperspectral image (area with maximum specularity) was located, segmented and labelled as the dominant region (A). By a simple dilation of this dominant region (*i.e.* the specular region), the neighbouring area (*i.e.* the diffuse region) surrounding the dominant region was marked, segmented and labelled as the surrounding region (B). As the diffuse reflectance should presumably be smooth, the mean diffuse reflectance $\bar{I}_D$ of both the dominant $[\bar{I}_D(x,\lambda)]_A$ and surrounding $[\bar{I}_D(x,\lambda)]_B$ regions were considered equal and the value of the scaling factor k was then calculated from the following equations:

$$[\bar{I}_D(x,\lambda)]_A = [\bar{I}_D(x,\lambda)]_B \qquad (7)$$

$$[\bar{I}(x,\lambda)]_A - k(x)\left[\bar{\beta}(x)\right]_A max\left(I_{max}(x,\lambda)\right) = [\bar{I}(x,\lambda)]_B - k(x)\left[\bar{\beta}(x)\right]_B max\left(I_{max}(x,\lambda)\right) \quad (8)$$

$$k(x) = \frac{[\bar{I}(x,\lambda)]_B - [\bar{I}(x,\lambda)]_A}{max\left(I_{max}(x,\lambda)\right).\left\{\left[\bar{\beta}(x)\right]_B - \left[\bar{\beta}(x)\right]_A\right\}} \quad (9)$$

To avoid post-processing of the image to obtain dominant and neighbouring regions, calculating the coefficient $k(x)$ in this study was determined by performing principle component analysis (PCA) of the input hyperspectral image yielding loadings of spectral wavelengths and scores for each single pixel in the hyperspectral image. Because the specular pixels usually cause the highest variability in the hyperspectral image, they are naturally captured in the first principle components. Thus, by finding the regions of the highest scores in the first PC score image, the mean and standard deviation of the specular pixels were calculated. The mean and standard deviation of all pixels having the highest scores in PC1 can be used as an estimate of coefficient $k(x)$ because they represents eigen-decomposition of the real contribution of the specular term in equation 6. The scores of the pure specular pixels isolated in the nonnegative PC1 score image were averaged and summed with three times their standard deviation as a reasonable estimate of $k(x)$. In other words, increasing the number of specular pixels in the score image will increase the value of the coefficient $k(x)$ and absence of specular pixels in the PC score image will lead this coefficient to equal zero meaning that the specular term is zero and the whole pixels are ideally diffuse pixels according to equation 6.

After calculating the coefficient $k(x)$, the second difficulty in calculating the specular term as declared in equation 6 was to calculate the coefficient $\beta(x)$ that depends on producing a specular-free image ($I_{SF}(x,\lambda)$) which provides partial separation of the specular component. In order to handle this issue, (Tan and Ikeuchi 2008) pioneered the idea of specular-free image which is a pseudo-diffuse image that has the same geometrical profile as the true diffuse component of the input image. It can be generated by subtracting the minimum reflectance image ($I_{min}(x,\lambda)$) of all bands from each pixel in the input hyperspectral image $I(x,\lambda)$ as:

$$I_{SF}(x,\lambda) = I(x,\lambda) - I_{min}(x,\lambda) \quad (10)$$

By substituting the reflectance image $I(x,\lambda) = I_{SF}(x,\lambda) + I_{min}(x,\lambda)$ from equation 10 into equation 6 $I_D(x,\lambda) = I(x,\lambda) - k(x)\beta(x)max\left(I_{max}(x,\lambda)\right)$, the diffuse component could be easily achieved as:

$$I_D(x,\lambda) = I_{SF}(x,\lambda) + I_{min}(x,\lambda) - k(x)\beta(x)max\left(I_{max}(x,\lambda)\right) \quad (11)$$

For pure specular pixels, the value of $k(x)max\left(I_{max}(x,\lambda)\right)$ could be set to one in all wavelengths yielding the pixel offset term τ_s as:

$$\tau_s = I_{min}(x,\lambda) - \beta(x) \quad (13)$$

Then, the specular coefficient $\beta(x)$ can be calculated as:

$$\beta(x) = I_{min}(x,\lambda) - \tau_s \qquad (14)$$

Because the specular-free image $I_{SF}(x,\lambda)$ visually appeared very close to the diffuse component image $I_D(x,\lambda)$ of the original image $I(x,\lambda)$, the pixel offset term τ_s could be safely set to a threshold T_2 that can generally distinguish pixels of high specularity. This threshold could be calculated from the minimum image $I_{min}(x,\lambda)$ as:

$$T_2 = \bar{I}_{min}(x,\lambda) + \eta\sigma_{I_{min}} \qquad (15)$$

where $\bar{I}_{min}(x,\lambda)$ and $\sigma_{I_{min}}$ are the mean and standard deviation of the minimum image $I_{min}(x,\lambda)$ for all pixels and η is a factor to express the specular degree of an image and it was set to $\eta = 0.5$ as proposed by Shen & Cai (2009). If the minimum value of a pixel is smaller than the threshold T_2, it should be a pixel with a diffuse reflectance value. By the knowing the coefficients $k(x)$ and $\beta(x)$, the specular and diffuse components can be easily calculated and separated from the original hyperspectral image (equation 6). Given an input of specular-contaminated hyperspectral image, the decomposing algorithm should result in two components, the diffuse and specular components. In Figure 2 are shown the key steps involved in resolving the original hyperspectral image into the diffuse and specular components.

2.5. Computational procedures

The complete steps of the proposed highlight removal method are outlined in Algorithm 1. The input of this algorithm is a single 3-D hypercube hyperspectral image (m columns × n rows × Ω wavelengths). To facilitate the subsequent processing steps, the hyperspectral image was reshaped into a 2-D matrix in the form of (m×n)×Ω in which each row stores the full spectrum of one pixel at all wavelengths Ω. In brief, the values of the minimum and maximum reflectance as well as the minimum and maximum thresholds were first determined and then used for calculating the specular coefficient '$\beta(x)$'. Then, principle component analysis was carried out on the 2D matrix of the hyperspectral image and the scores of the first principle component were then used to calculate the adjusting coefficient '$k(x)$'. Finally, the diffuse and specular components were calculated from equation 11 and 5, respectively. The final step in the procedure includes folding the diffuse and specular images into 3D forms having the same dimensions as the original hyperspectral image implying that any sub-image at a certain wavelength λ of the original hyperspectral image is decomposed into diffuse and specular images at this wavelength.

Algorithm 1: Pseudo-code of the algorithm developed for decomposing a hyperspectral image into diffuse and specular components

---

[Id, Is] = Algorithm ALG (I)
start
1 Read the raw hypercube hyperspectral image 'I' in a 3-D form of dimensions 'm×n×Ω'
2 Unfold the hypercube from 3-D form into a 2-D matrix of dimensions '(m×n)×Ω′
3 Scale the 2-D matrix to have reflectance values from 0 to 1.
4 Get the minimum image 'Imin' via calculating the minimum reflectance throughout all wavelengths
5 Get the maximum image 'Imax' via calculating the maximum reflectance throughout all wavelengths
6 Calculate the minimum threshold $T_2 = \tau_s$ using equation 15
7 Calculate the diffuse coefficient $\beta(x)$ using equation 14
8 Calculate the maximum value in 'Imax' and the maximum threshold T_2 for segmenting specular pixels
9 Determine the specular-free image 'Isf' using equation 10
10 Perform principle component analysis of the hypercube and extract the first principle component 'PC1'
11 Fold the column vector 'PC1' into a 2D score image
12 while PC1>0 'non-negative constraint'
13 Scale the scores in PC1 from 0 to 1
14 Calculate the mean and standard deviation of the highest specular pixels in PC1
15 Calculate the adjusting coefficient 'k(x)′
16 end while
17 Determine the diffuse reflectance component 'Id' using equation 11
18 Determine the specular reflectance component 'Is' using equation 5
19 Fold the resulting components into 2D form as shown in Figure 2
20 Return Id and Is
end Algorithm ALG

2.6. Textual analysis

The effect of the proposed method in mitigating specularity problem could be evaluated by carrying out texture analysis of the image to identify the evenness of reflectance before and after specular removal. Due to the presence of specular highlights that appeared either on the object itself or in the background, the spectral signatures were drastically affected in a manner not related to the intrinsic properties of the food samples. If the proposed method was efficient in removing the specular highlights from the affected pixels in the object or in the background, the resulting spectrum of these pixels should be completely uniform throughout the spectrum. Thus, a square window (100×100 pixels) was cropped from the object and another window was also cropped from the background in the hyperspectral image as shown Figure 8b to discover the textural change before and after specular

removal. Textural characteristics refer to variations in the brightness values, which is very useful in estimating the effect of specular removal routine applied in this study. The Grey Level Co-occurrence Matrix (GLCM) technique was used to calculate four different textural features (*i.e.* Contrast, Homogeneity, Angular Second Moment 'ASM' and Correlation) using the formulas shown below (Huang et al., 2014; Jiang et al., 2019). For the sake of simplicity, only two parameters (contrast and homogeneity) were shown in this study to demonstrate the effect of the proposed method of specular removal in the evenness of the regions that previously affected by specular problem. Images having a uniform reflectance values in the affected pixels after being treated by specular removal routine should present low level of contrast and high level of homogeneity. In general, these texture parameters were determined at different distances (from $D = 1$ to $D = 10$) for each pixels in the GLCM and then averaged to give only one value at each direction (ElMasry et al., 2007). Then, a co-occurrence matrix is a square matrix with elements corresponding to the relative frequency ($P_{i,j}$) of occurrence of pairs of grey level of pixels separated by a certain distance (D) in a given direction (0, 45, 90, or 135°). Each entry (i,j) in the GLCM corresponds to the number of occurrences of the pair of grey levels i and j which are a distance D apart in the image (Malegori et al., 2016; Jiang et al., 2019).

$$Contrast = \sum_{i,j=0}^{N-1} P_{i,j}(i-j)^2 \qquad (16)$$

$$Homogenity = \sum_{i,j=0}^{N-1} \frac{P_{i,j}}{1+(i-j)^2} \qquad (17)$$

$$ASM = \sum_{i,j=0}^{N-1} {P_{i,j}}^2 \qquad (18)$$

$$Correlation = \frac{\sum_{i,j=0}^{N-1}(ij)P_{i,j} - \mu_x\mu_y}{\sigma_x\sigma_y} \qquad (19)$$

where $\mu_x, \mu_y, \sigma_x,$ and σ_y are the means and standard deviations of the sums of rows and columns in the GLCM matrix, respectively.

3. Results and Discussion

3.1. Separation of diffuse and specular components

According to the dichromatic model and equation 5 explained above, the acquired hyperspectral image $I(x,\lambda)$ with specularity highlight problem should be resolved into the diffuse $I_D(x,\lambda)$ and specular $I_S(x,\lambda)$ components. The diffuse component shows the real reflectance related to the intrinsic spectral properties of the objects in the scene; meanwhile the specular component shows the areas of peculiar reflectance across the spectrum. Therefore, the success of any specular removal tool is evaluated based on its ability of separating these particular components. As shown in Figure 3, the specularity removal method applied in this study was able to separate both diffuse and specular components from a raw hyperspectral image of mixed fruits and vegetables acquired in the spectral range of 400-1000 nm and with spatial dimensions of 1000×900 pixels and 300 spectral bands. In

fact, these two components should be separated at every single band of the hyperspectral image meaning that every sub-image in the hyperspectral image was resolved into diffuse and specular components. Due to the limitation of space, only a selected number of bands at 450, 600, 800 and 950 nm are shown covering wavelengths in the spectral range (400-1000 nm). The images shown in Figure 3 demonstrate how the developed method had the capacity in separating the raw hyperspectral image (Figure 3a) of mixed fruits and vegetables into the diffuse (Figure 3b) and specular (Figure 3c) component images. As shown in Figure 3, it is very clear to notice that the appearance of the objects having the specular problem enhanced significantly and most of the specular regions were potentially alleviated. Because it is not possible to visualize the hyperspectral image in its current 3-dimensional hypercube, a pseudo-colour image could be created to see the effect of the specular removal method on the overall appearance of the hyperspectral image. Thus, when three different bands selected from the hyperspectral images across the spectrum were concatenated altogether, a pseudo-colour image was formed. In this example, the bands at 640, 550 and 460 nm were chosen to represent the red, green and blue channels to compose a pseudo-RGB image shown in the last column of Figure 3.

With the same routine, the proposed method was also very efficient in removing specular highlights from a hyperspectral image of cured ham slices we acquired ourselves using the same hyperspectral imaging system in the spectral range of 400-1000 nm. This image has spatial dimensions of 900×1650 pixels and 300 spectral bands. It is very obvious to notice from Figure 4 that the specular spots appeared in some parts of the image have been removed from all bands, leaving diffuse only reflections in every image slice at different bands without any sign of specular highlights. Most interestingly, the background pixels suffered from specularity became more homogenous after removing specular reflectance components from the image that will facilitate all subsequent processing steps in the image such as segmentation and spatial feature extraction.

Figure 5 shows some hyperspectral images treated by the proposed method for removing specular highlights from the images. For the sake of simplicity, the original spectral images (first row in Figure 5) and the resulting diffuse only reflectance images (the second row in Figure 5) were presented as pseudo-colour images in each to evaluate the process before and after specular removal treatment. The specular reflectance component images were also presented in the third row of Figure 5 to locate the specular highlight pixels in each image. As explicitly exhibited in images shown in Figure 5, the proposed method had a substantial capacity in removing specular highlights despite the spectral range and the acquisition mode of the spectral images. The method was successful in removing specular highlights from hyperspectral images of band-interleaved by line (bil) format (Figures 5-1, 5-2, 5-3 and 5-4), from a hyperspectral image in band-interleaved by pixel (bip) format (Figure 5-5), from a hyperspectral image in band sequential (bsq) format (Figure 5-6) and from a multispectral image acquired wavelength by wavelength sequentially (Figure 5-7).

3.2. Effect of specular removal on spectral signatures

To demonstrate the effect of the proposed specularity removal method on the overall quality of the image, spectral signatures were extracted from different zones in the hyperspectral image especially from those zones that suffer from specularity problems. Figure 6 shows the spectral signatures of six different spots in the hyperspectral image of mixed fruits and vegetables. The diffuse and specular zones were identified with the aid of the specular component of the same image shown in Figure 3c. Four spectra were extracted from four different specular points (P1, P2, P3 and P4) and two spectra were extracted from two other areas that did not show specularity (P5 and P6). The highlight removal method separates the specular and diffuse components at every single pixel position to get the diffuse image. Because the spectrum at any pixel in the image has been defined as the linear combination of the specular highlight spectrum and the diffuse spectrum (Tan, Nishino et al. 2004; An, Suo et al. 2015), the pixels that exhibited specularity should obviously have lower reflectance values after treatment due to removing the specular components from those pixels. Therefore, the spectra of specular points P1, P2, P3 and P4 that exhibited specularity highlights showed lower reflectance values along the whole spectral range after being treated by specularity removal method. In Figure 6b, the raw spectra of specular pixels were plotted in solid lines and the treated spectra resulting after specularity removal of the same pixels were plotted in dash lines. As the spectra of points P5 and P6 were extracted from diffuse pixels (pixels that did not show specularity highlight problem), their spectral signatures did not change after being treated and the spectra of those points were noticeably identical before and after treatment as shown in Figure 6c. Similarly, the spectral signatures of specular pixels (A1 and A2) in the ham image shown in Figure 6d were remarkably reduced after being treated with the specular removal method as shown in Figure 6e. More interestingly, the spectral pattern of fat pixel (A3) remained without change (Figure 6f) as this area contains only diffuse pixels without any symptoms of specularity highlights as declared in its specular component image shown in Figure 5c.

The developed method was also evaluated in regards to the change occurred in the location of the absorption bands in the spectrum. As shown in Figure 6b, the specularity removal treatment only reduces the magnitude of reflectance (due to removing the specular component from the image) while preserving the shape and the spectral patterns of the object being examined. For instance, the absorption band at 680 nm in green banana (P3) and lettuce leaf (P4) is a typical absorption feature of Chlorophyll, which is still well preserved after the specularity removal step (Fu, Tan et al. 2006).

Figure 7 shows the spectral patterns of all pixels along some horizontal lines in both raw hyperspectral image and treated image. In general, specular removal treatment led to a reduction in the pixel intensity at specular points and steadiness of pixel intensity at the diffuse points. For instance, the maximum relative reflectance of specular pixels along the blue horizontal line drawn in

the mixed fruit image shown in Figure 7a reduced from 0.95 as shown in Figure 7c to only 0.82 after being treated with specular removal procedure as shown in Figure 7d. Similarly, the maximum relative reflectance of specular pixels along the yellow horizontal line passing through tomato fruit in the mixed fruit image shown in Figure 7a reduced from 0.75 as shown in Figure 7e to only 0.65 after being treated with specular removal procedure as shown in Figure 7f. Moreover, as shown in Figure 7j, the spectral signatures of background pixels along the horizontal line in the treated meat image shown in Figure 7g become more homogeneous and flat compared to the spectral signatures of the same pixels in the original hyperspectral image (Figure 7h). The maximum relative reflectance of specular pixels in the background regions of Figure 7g declined from 0.68 as shown in Figure 7h to only 0.54 after specular removal treatment as shown in Figure 7j. Such enhanced form of the background pixels will facilitate all subsequent image-processing operations such as segmentation or feature extraction.

3.3. Textural analysis

Besides the overall visual assessment explained above, it is important to calculate some objective parameters to evaluate the quality of the resulting image after being treated with the specular removal method. Figure 8a shows the means of two texture parameters (contrast and homogeneity) extracted from GLCM at different directions (0, 45, 90 and 135°) of the background region in the hyperspectral image of meat sample shown in Figure 7g at different bands in the spectral region of 900-1700 nm. As appeared in Figure 8, the hyperspectral image at different bands (e.g. 950, 1200, 1300 and 1600 nm) is characterized by high contrast and low homogeneity especially in the background portions due to specular highlight problem. However, the image after specularity removal exhibited lower contrast and higher homogeneity compared with the untreated image as clearly shown in texture features illustrated in Figure 8a.

On the other hand, alleviating specularity problem becomes more critical if the specular highlight appeared in the examined object itself inside the image. This is because specularity not only affects all extracted spectral features but also it leads to ambiguous description of this object. For instance, when the specularity removal pre-treatment was applied on a hyperspectral image of a dry-cured ham sample with a specular zone located in the ham sample itself, the result was very optimistic in alleviating the specular problem and improving the quality of the spectral images throughout the whole spectral range. In a similar way, the textural features (contrast and homogeneity) extracted from GLCM of the central region of specular highlights area were substantially improved as shown in Figure 8b. The textural analysis results indicated that the specular removal treatment provided images with less contrast and high homogeneity at all bands.

3.4. Comparison with other specular removal techniques

The huge amount of pixels in a hyperspectral image does impose great challenges on the aspects of model expression and computational efficiency (Zheng, Sato et al. 2015). Therefore, the method proposed in this work was compared with Shen and Cai's method (Shen & Cai, 2009) that does not involve iterative process either. The two methods were compared qualitatively based on the overall separation of the specular component and quantitatively based on the running time and peak signal to noise ratio (PSNR).

To visually compare the outcomes resulting from both methods, Figure 9 shows the treated hyperspectral images after removing the specular component from the original hyperspectral images. Six spectral images of different agro-food products (fat, loin, ham slices, M&M balls, fruits and vegetables and yellow pepper) were used in such comparison (Figure 9). Instead of comparing both methods at each single waveband, the pseudo-colour images were only presented to facilitate the comparison. It is very clear to notice that both methods were very efficient in removing the specular highlights appeared in all spectral images. The proposed method outperformed the Shen and Cai's method in most of the presented spectral images. This could be clearly noticed from the graphs of the spectral signatures presented in Figure 9 in which the proposed method provides lower magnitudes of reflectance in all wavelengths, meaning that the proposed method removed more highlights from the original image. This finding is obvious in case of the multispectral image of the yellow pepper presented in Figure 9f and their corresponding spectral signatures. Where the proposed method largely mitigated the specularity highlights from this image, the image resulted from Shen and Cai's method still suffers from some specularity in some pixels. However, the results of both methods are comparable to each other and should be evaluated numerically based on the running time and PSNR values.

Table 1 summarizes the running time of both methods in treating the six spectral images performed on a desktop computer of core i5-3470 CPU, 3.2 GHz and 14.0 GB of memory. Moreover, the global and regional PSNR values of both specular reflection separation methods were also calculated and presented in Table 1. The global values of PSNR were calculated for the whole spectral images after being treated by both methods of specularity removal, meanwhile the regional values of PSNR were only calculated from the specular regions in the images. As can be seen, the proposed method had higher PSNR compared to Shen and Cai's method indicating that the proposed method is a bit more robust and effective in removing the specularity highlights from all tested hyperspectral and multispectral images except the M&M image. This may be ascribed to the band-interleaved-by-pixel (bip) format of this image or to the small size of the objects in this image. However, the running times of the proposed method are relatively slower than Shen and Cai's method under Matlab environment but fortunately this kind of pre-treatment methods is not usually applied in real-time applications in

hyperspectral images. If the important wavelengths were carefully selected from the full spectrum, this constraint would not be a problem in rapid processing regimes.

4. Conclusion

One of the most common problems encountered in most hyperspectral and multispectral images of food objects and other biomaterials is the specularity highlights. The analysis of the examined images indicated that the proposed method accurately separate reflection components for different hyperspectral and multispectral images even when images are acquired under different acquisition modes and configurations. In comparison with the existing methods used for removing specularity highlights, the proposed method is more robust and preferable because it does not require object segmentation, iterative operation and user interference for highlights localization. The specular removal routine helped in enhancing the reflectance features at all wavebands throughout the whole spectrum leading to consistent spectral data and developing classification or prediction models. Although the running time is a bit longer, it provides better performance in terms of the quality of specular removal and higher peak signal to noise ratio (PSNR). Thus, the proposed highlight removal method looks promising for all spectral imaging scenarios and opens new venues of different application especially those related to non-destructive evaluation of food products. Improving the image acquisition, alleviating specularity highlight problem and using the samples without prior preparation will help in applying this state-of-the art spectral imaging method for a wide range of tasks in food quality evaluation processes in on-line industrial applications.

Acknowledgements

Authors significantly acknowledge the financial support from the Marie Sklodowska-Curie COFUND P-SPHERE project under the European Union's Horizon 2020 research and innovation programme with grant agreement No665919 and the Distinguished Scientist Fellowship Program (DSFP) King Saud University.

References

Achata, E. M., Inguglia, E. S., Esquerre, C. A., Tiwari, B. K. & O'Donnell, C. P. (2019). Evaluation of Vis-NIR hyperspectral imaging as a process analytical tool to classify brined pork samples and predict brining salt concentration. *Journal of food engineering*, 246, 134-140.

Akashi, Y., & Okatani, T. (2016). Separation of reflection components by sparse non-negative matrix factorization. *Computer Vision and Image Understanding*, 146(1), 77-85.

529 An, D., Suo, J., Wang, H. & Dai, Q. (2015). Illumination estimation from specular highlight in a
530 multi-spectral image. *Optics express*, 23(13), 17008-17023.

531 Artusi, A., Banterle, F. & Chetverikov, D. (2011). A survey of specularity removal methods. In
532 Computer Graphics Forum (Vol. 30, pp. 2208-2230): Wiley Online Library, Blackwell
533 Publishing Ltd., Oxford, UK.

534 Bochko, V. & Parkkinen, J. (2005). Highlight analysis using a mixture model of probabilistic PCA. In
535 Proceedings of the 4th WSEAS International Conference on Signal Processing, Robotics and
536 Automation (pp. 15): World Scientific and Engineering Academy and Society (WSEAS).

537 Chao, K., Yang, C.-C., Kim, M. S., & Chan, D. E. (2008). High throughput spectral imaging system
538 for wholesomeness inspection of chicken. *Applied Engineering in Agriculture*, 24(4), 475–485.

539 ElMasry, G. & Nakauchi, S. (2016). Image analysis operations applied to hyperspectral images for
540 non-invasive sensing of food quality-A comprehensive review. *Biosystems Engineering*,
541 142(1), 53-82.

542 ElMasry, G., Sun, D.-W. & Allen, P. (2013). Chemical-free assessment and mapping of major
543 constituents in beef using hyperspectral imaging. *Journal of Food Engineering*, 117(2), 235-
544 246.

545 ElMasry, G., Sun, D. W., Kamruzzaman, M., Barbin, D. & Allen, P. (2012). Hyperspectral imaging-A
546 new era of applications in non-destructive sensing of meat quality. *NIR news*, 23(6), 9-14.

547 ElMasry, G., Wang, N., ElSayed, A. & Ngadi, M. (2007). Hyperspectral imaging for nondestructive
548 determination of some quality attributes for strawberry. Journal of Food Engineering, 81(1), 98-
549 107.

550 Fu, Z., Tan, R. T. & Caelli, T. (2006). Specular free spectral imaging using orthogonal subspace
551 projection. In Proceedings of the 18th International Conference on Pattern Recognition
552 (ICPR'06) (Vol. 1, pp. 812-815). IEEE, Hong Kong, China.

553 Guo, J., Zhou, Z. & Wang, L. (2018). Single Image Highlight Removal with a Sparse and Low-Rank
554 Reflection Model. In Proceedings of the European Conference on Computer Vision (ECCV
555 2018) (pp. 268-283). Munich, Germany.

556 Hamid, J.V.R. (2013). Estimating the colour of the illuminant using specular reflection and exemplar-
557 based method. PhD Dissertation, Simon Fraser University, British Columbia, Canada.

558 He, Y., Khanna, N., Boushey, C. J. & Delp, E. J. (2012). Specular highlight removal for image-based
559 dietary assessment. In 2012 IEEE International Conference on Multimedia and Expo
560 Workshops (pp. 424-428). IEEE, Melbourne, VIC, Australia.

561 Huang, X., Liu, X., & Zhang, L. (2014). A multichannel gray level co-occurrence matrix for
562 multi/hyperspectral image texture representation. *Remote Sensing*, 6(9), 8424-8445.

563 Jiang, H., Yoon, S. C., Zhuang, H., Wang, W., Li, Y., & Yang, Y. (2019). Integration of spectral and
564 textural features of visible and near-infrared hyperspectral imaging for differentiating between
565 normal and white striping broiler breast meat. *Spectrochimica Acta Part A: Molecular and*
566 *Biomolecular Spectroscopy*, 213, 118-126.

567 Kavusi, S. & ElGamal, A. (2004). Quantitative study of high-dynamic-range image sensor
568 architectures. In: Sensors and Camera Systems for Scientific, Industrial, and Digital
569 Photography Applications, Proceeding of SPIE Electronic Imaging Conference, International
570 Society for Optics and Photonics, 5301, 264-275.

571 Khan, H. A., Thomas, J.-B. & Hardeberg, J. Y. (2017). Analytical survey of highlight detection in
572 color and spectral images. In International Workshop on Computational Color Imaging (pp.
573 197-208). March 2017, Milan, Italy.

574 Koirala, P., Pant, P., Hauta-Kasari, M. & Parkkinen, J. (2011). Highlight detection and removal from
575 spectral image. *Journal of the Optical Society of America A (JOSA A)*, 28(11), 2284-2291.

576 Lehmann, T. M. & Palm, C. (2001). Color line search for illuminant estimation in real-world scenes.
577 *Journal of the Optical Society of America A (JOSA A)*, 18(11), 2679-2691.

578 Martin, D. (2007). A practical guide to machine vision lighting. Midwest Sales and Support Manager,
579 Adv Illum2007, 1-3.

580 Malegori, C., Franzetti, L., Guidetti, R., Casiraghi, E. & Rossi, R. (2016). GLCM, an image analysis
581 technique for early detection of biofilm. *Journal of Food Engineering*, 185, 48-55.

582 Nakauchi, S., Nishino, K. & Yamashita, T. (2012). Selection of optimal combinations of band-pass
583 filters for ice detection by hyperspectral imaging. *Optics express*, 20(2), 986-1000.

584 Nayar, S. K., Fang, X.-S. & Boult, T. (1997). Separation of reflection components using color and
585 polarization. *International Journal of Computer Vision*, 21(3), 163-186.

586 Nguyen, T., Vo, Q.N., Yang, H.-J., Kim, S.-H. & Lee, G.-S. (2014). Separation of specular and
587 diffuse components using tensor voting in color images. *Applied optics*, 53(33), 7924-7936.

588 Nguyen-Do-Trong, N., Dusabumuremyi, J.C. & Saeys, W. (2018). Cross-polarized VNIR
589 hyperspectral reflectance imaging for non-destructive quality evaluation of dried banana slices,
590 drying process monitoring and control. *Journal of food engineering*, 238, 85-94.

591 Park, B., Lawrence, K, C., Windham, W. R. & Buhr, R.J. (2002). Hyperspectral Imaging for
592 Detecting Fecal and Ingesta Contaminants on Poultry Carcasses. *Transactions of ASAE*, 45(6),
593 2017-2026.

594 Shen, H.-L. & Cai, Q.-Y. (2009). Simple and efficient method for specularity removal in an image.
595 *Applied optics*, 48(14), 2711-2719.

596 Shen, H.-L. & Zheng, Z.-H. (2013). Real-time highlight removal using intensity ratio. *Applied optics*,
597 52(19), 4483-4493.

598 Shen, H.-L., Zhang, H.-G., Shao, S.-J. & Xin, J. H. (2008). Chromaticity-based separation of
599 reflection components in a single image. *Pattern Recognition*, 41(8), 2461-2469.

600 Sivertsen, A. H. (2011). Automatic inspection of cod (Gadus Morhua L.) fillets by hyperspectral
601 imaging. PhD Dissertation, the Artic University of Norway.

602 Suktanarak, S. & Teerachaichayut, S. (2017). Non-destructive quality assessment of hens' eggs using
603 hyperspectral images. Journal of food engineering, 215, 97-103.

604 Suo, J., An, D., Ji, X., Wang, H. & Dai, Q. (2016). Fast and high quality highlight removal from a
605 single image. *IEEE Transactions on Image Processing*, 25(11), 5441-5454.

606 Tan, R. T. & Ikeuchi, K. (2008). Separating reflection components of textured surfaces using a single
607 image. *IEEE Transactions on Pattern Analysis and Machine Intelligence*, 27(2), 178-193.

608 Tan, R.T., Nishino, K. & Ikeuchi, K. (2004a). Color constancy through inverse-intensity chromaticity
609 space. *Journal of the Optical Society of America A (JOSA A)*, 21(3), 321-334.

610 Tan, R.T., Nishino, K. & Ikeuchi, K. (2004b). Separating reflection components based on
611 chromaticity and noise analysis. *IEEE transactions on pattern analysis and machine*
612 *intelligence*, 26(10), 1373-1379.

613 Washburn, K. E., Stormo, S. K., Skjelvareid, M. H. & Heia, K. (2017). Non-invasive assessment of
614 packaged cod freeze-thaw history by hyperspectral imaging. *Journal of Food Engineering*, 205,
615 64-73.

616 Wold, J.P., O'Farrell, M., Høy, M. & Tschudi, J. (2011). On-line determination and control of fat
617 content in batches of beef trimmings by NIR imaging spectroscopy. *Meat science*, 89(3), 317-
618 324.

619 Yamamoto, T., Kitajima, T. & Kawauchi, R. (2017). Efficient improvement method for separation of
620 reflection components based on an energy function. In 2017 IEEE International Conference on
621 Image Processing (ICIP) (pp. 4222-4226). IEEE, Beijing, China.

622 Yang, F., Tang, X., Hu, B., Wei, R., Kong, L. & Li, Y. (2016). A Method of Removing Reflected
623 Highlight on Images Based on Polarimetric Imaging. *Journal of Sensors*, 2016, 1-8.

624 Yang, Q., Tang, J., & Ahuja, N. (2015). Efficient and robust specular highlight removal. *IEEE*
625 *transactions on pattern analysis and machine intelligence*, 37(6), 1304-1311.

626 Yoon, K.-J., Choi, Y. & Kweon, I. S. (2006). Fast separation of reflection components using a
627 specularity-invariant image representation. In IEEE 2006 International Conference on Image
628 Processing (pp. 973-976). Atlanta, GA, USA: IEEE.

629 Zheng, Y., Sato, I. & Sato, Y. (2015). Illumination and reflectance spectra separation of a
630 hyperspectral image meets low-rank matrix factorization. In Proceedings of the 28th IEEE
631 Conference on Computer Vision and Pattern Recognition (pp. 1779-1787). IEEE, Boston, MA,
632 USA.

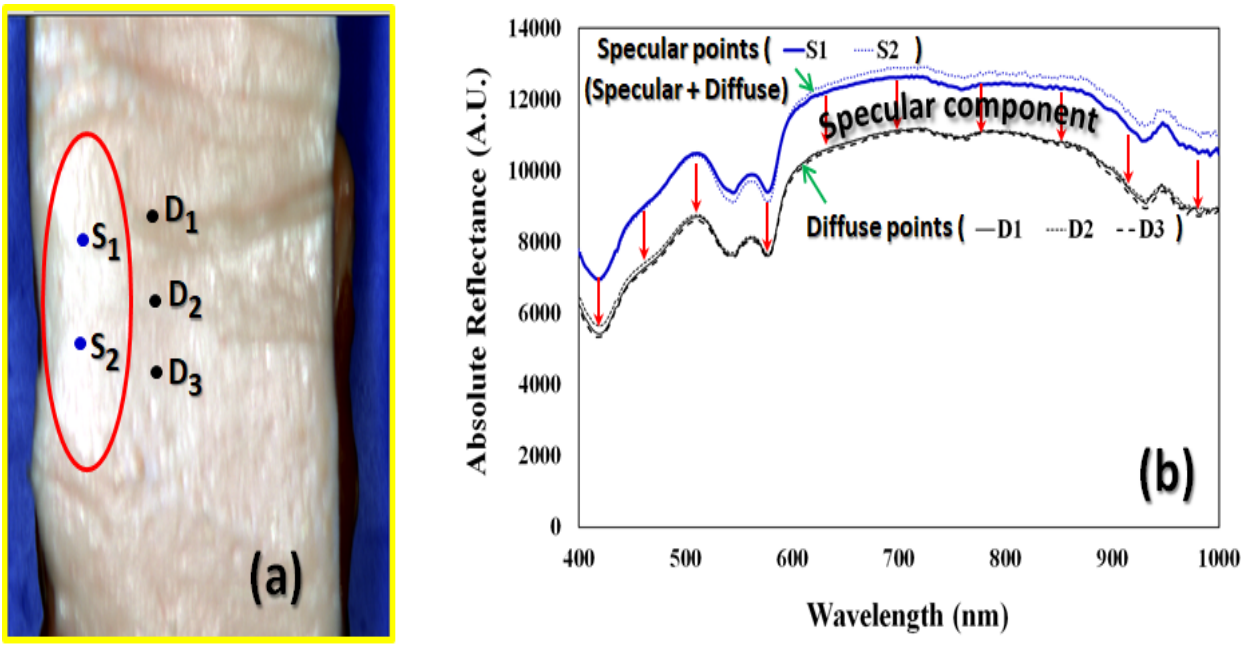

Figure 1 (a) Pseudo-colour image rendered at 640 nm, 550 nm and 460 nm from a hyperspectral image acquired in the spectral range of 400-1000 nm for a homogeneous fat layer having a specular zone marked with a red ellipse at the left-hand side of the image and (b) the corresponding spectral signatures of three diffuse points (D_1, D_2 and D_3) and two specular points (S_1 and S_2) inside the specular region adjacent to the diffuse points. Specular highlights can be observed in the highly reflected zone where it washed out the spatial and spectral information in this particular spot of the image. After removing specular component from the image, the five points (D_1, D_2, D_3, S_1 and S_2) will identically exhibit the same spectral patterns similar to the diffuse points as the arrow indicated (b).

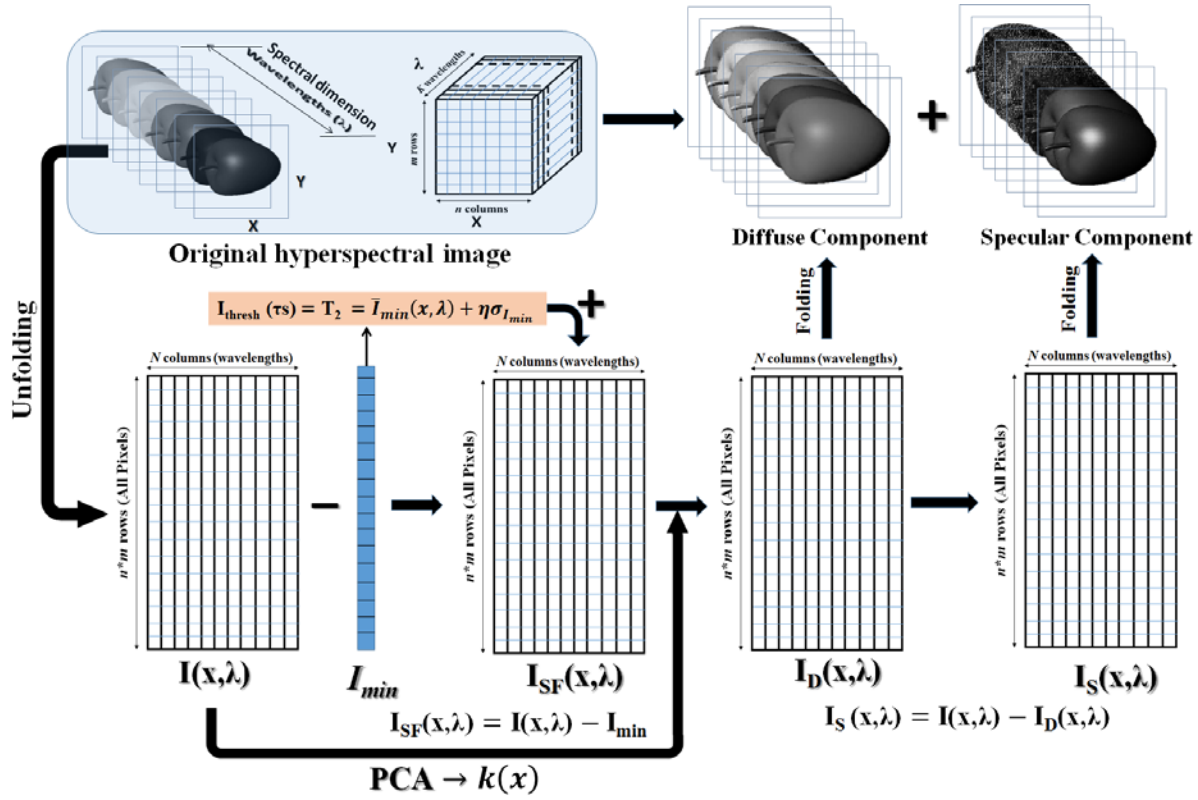

644

645 Figure 2 A schematic diagram of the decomposition process of a hyperspectral image $I(x,\lambda)$ having a
646 specular highlight problem into diffuse $I_D(x,\lambda)$ and specular $I_S(x,\lambda)$ components.

647

648

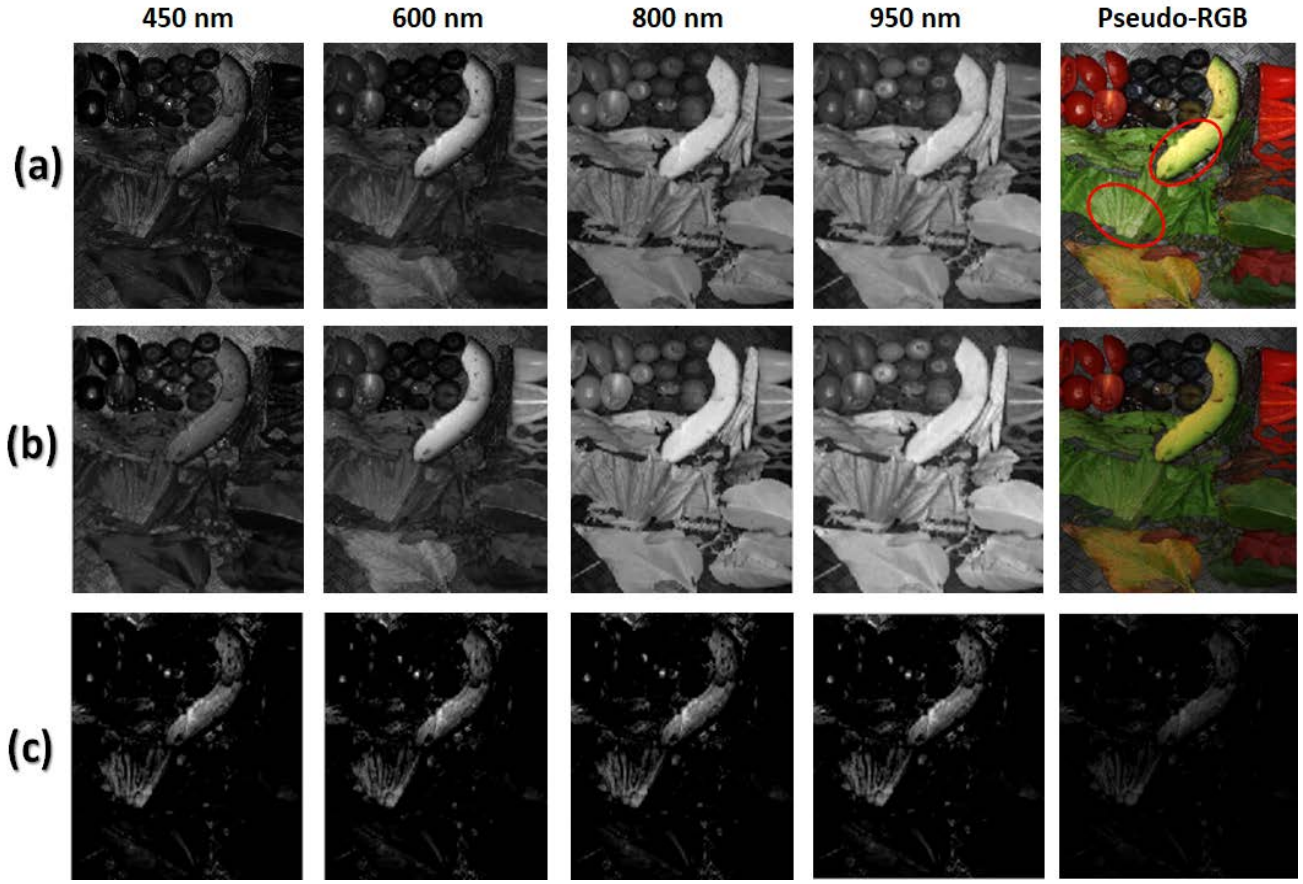

Figure 3 (a) A raw hyperspectral image (400-1000 nm) of mixed fruits and vegetables at some selected bands across the spectrum and their corresponding diffuse (b) and specular components (c) at the same bands. A pseudocolour image shown in the right-hand column was created by rendering the raw, diffuse and specular images at three different bands (640, 550 and 460 nm) to represent the red, green and blue channels of the pseudocolour image. Some specular zones are marked in red ellipses in the original image.

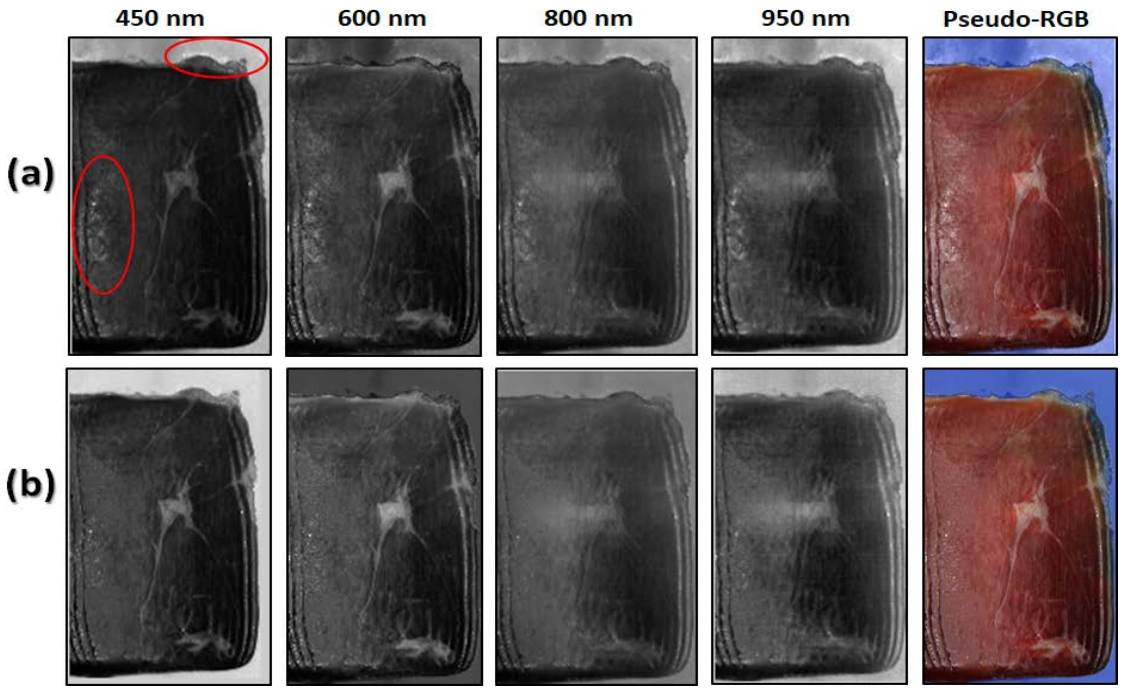

Figure 4 (a) A raw hyperspectral image of dry-cured ham slices at some selected bands across the spectrum with some specular highlights zones appeared in all bands and (b) the corrected image with only diffuse component after specular removal from all bands. Some specular zones are marked in red ellipses in the original image.

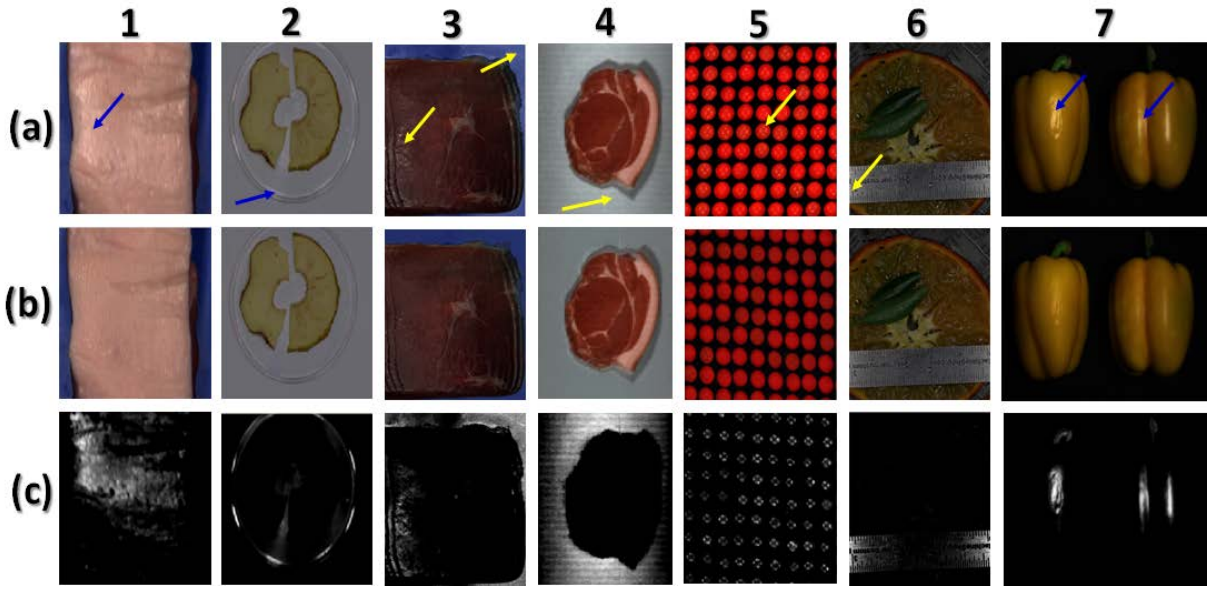

Figure 5 Effectiveness of the proposed method in removing specular highlights from hyperspectral and multispectral images. (a) raw spectral images, (b) diffuse component images after removing specular components and (c) specular component images. Arrows point to the location of specular highlights in the image as shown in the specular component images. (1-3) hyperspectral image of 300 bands (400-1000 nm) in 'bil' format for a piece of meat, a slice of apple, and dry-cured ham slices, (4) a hyperspectral image of 237 bands (900-1700 nm) in 'bil' format for a piece of meat, (5) a hyperspectral image of 80 bands (400-880 nm) in 'bip' format for M&M balls, (6) a hyperspectral image of 462 bands (400-1000 nm) in 'bsq' format for a piece of citrus and a metal ruler, and (7) a multispectral image of 30 bands (400-700 nm) for artificial and real peppers.

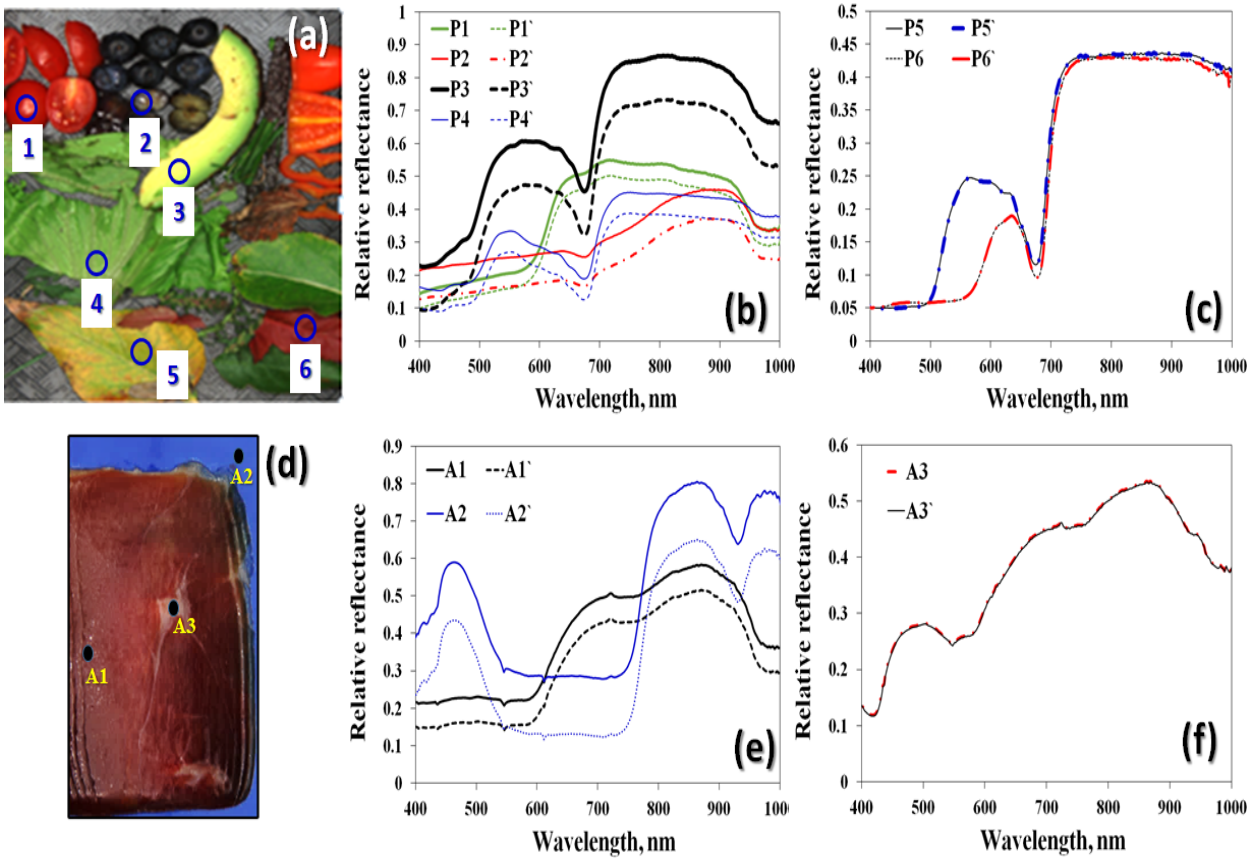

Figure 6 (a) a hyperspectral image with marked six points, (b) spectral signatures of four different specular points (P1, P2, P3 and P4) before and after specular removal treatment, (c) the spectral signatures of diffuse points P1 and P2 (that do not exhibit specularity) are typically identical before and after specular removal treatment, (d) a hyperspectral image of dry-cured ham slices, (e) spectral signatures of two specular points (A1 and A2) before and after specular removal treatment, (f) the spectral signature of a diffuse point A3 of fat pixels is typically identical before and after specular removal treatment. Raw spectra of the marked points were plotted in solid lines and the corresponding highlight removed spectra of the same points were plotted in dash lines.

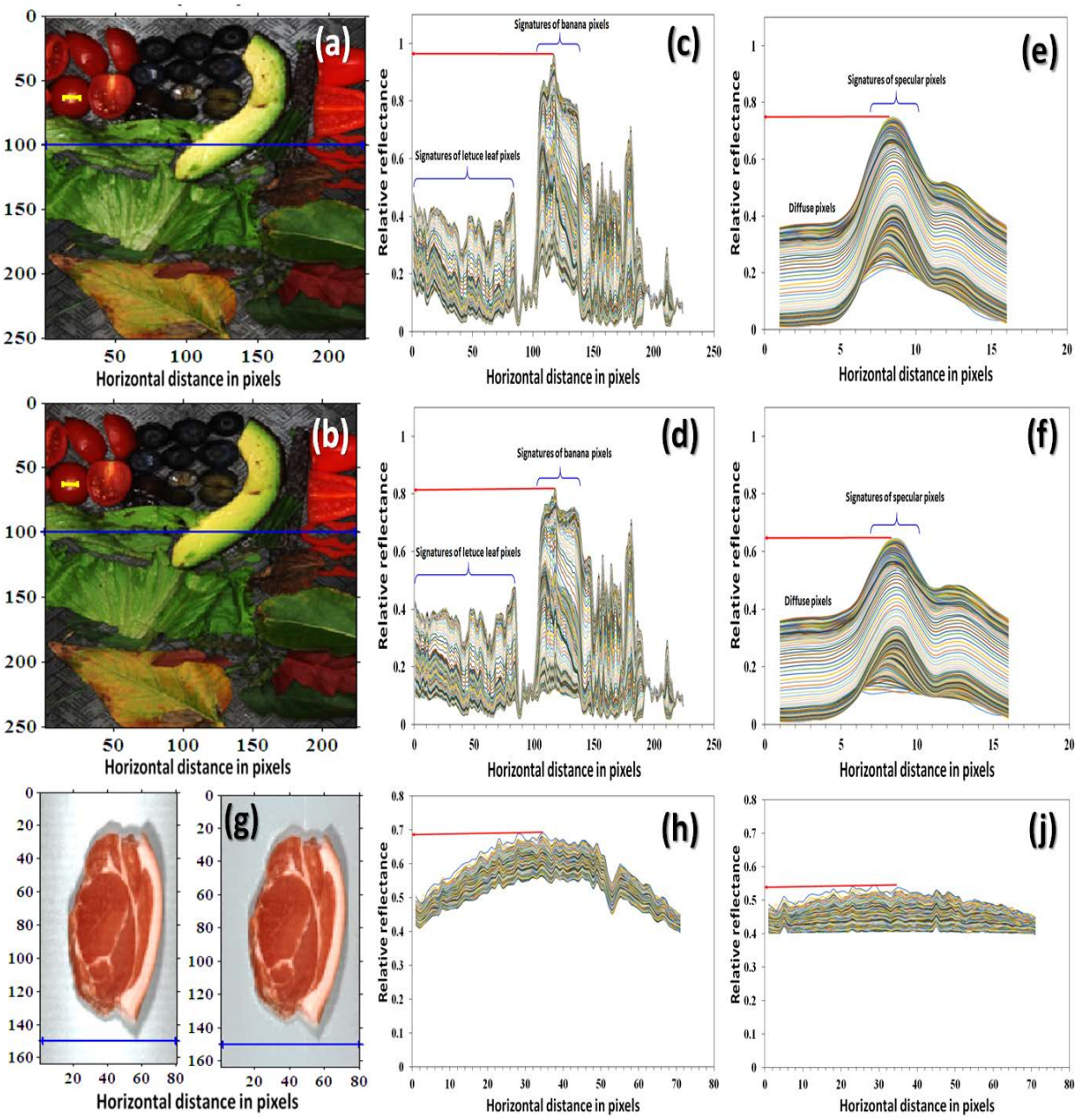

Figure 7 Spectral patterns of all pixels along horizontal lines in both raw and treated hyperspectral image (a, b & g). Specular removal treatment led to a reduction in the pixel intensity at highlight points and steadiness of pixel intensity at the diffuse points. (c & d) spectral signatures of all pixels along the long blue horizontal line in the raw and treated mixed fruit image, (e & f) spectral signatures of all pixels along the short yellow horizontal line in the raw and treated image, (h) raw spectral signature of background pixels along the horizontal blue line drawn in raw meat image (g), and (j) spectral features of the background pixels along the horizontal blue line drawn in the treated meat image.

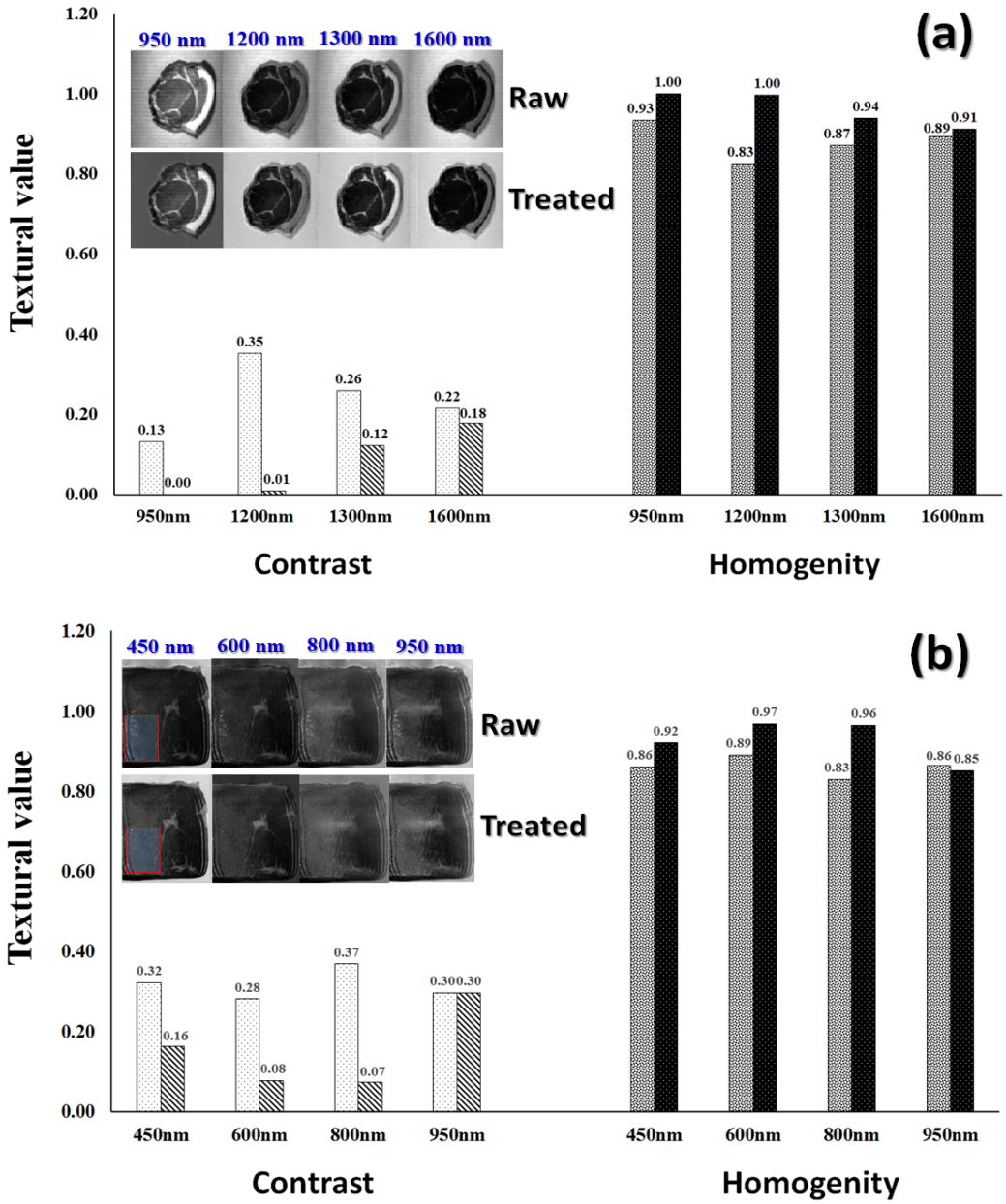

Figure 8 Texture features calculated by GLCM method for raw and treated hyperspectral images for (a) background pixels in the hyperspectral image of meat sample and (b) central region of specular highlights appeared in the hyperspectral image of the dry-cured ham sample. The raw and corrected images at some bands in the spectrum are shown in the corner of each graph and the red square locates the position at which the texture values were calculated.

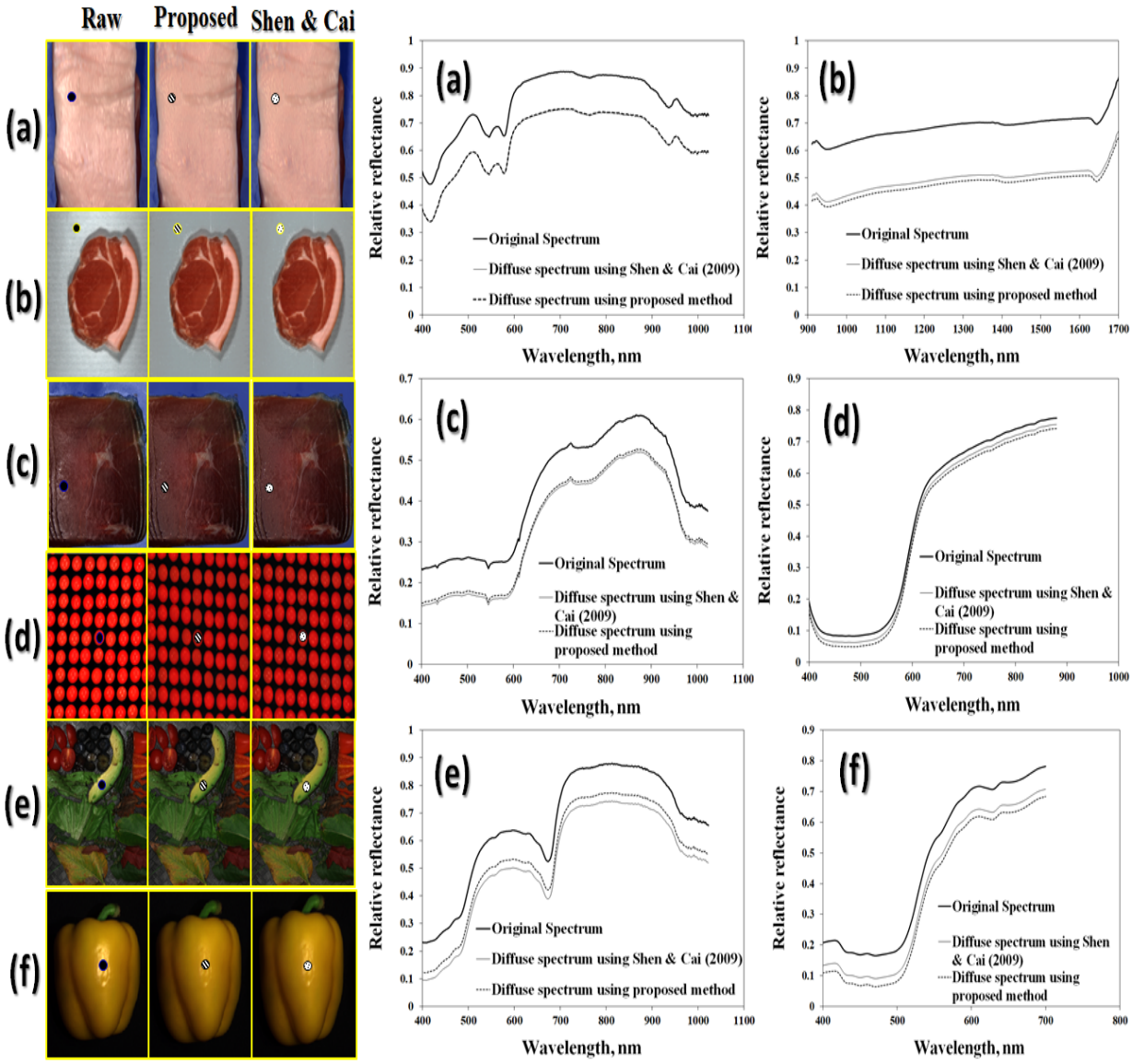

Figure 9 Comparison between the proposed method and the method of Shen and Cai (2009) in removing specular highlights from hyperspectral images of different agro-food materials. Graphs (a-f) are the corresponding spectral signatures of specular areas before and after specularity removal treatment by both methods from hyperspectral images of fat, loin, ham slices, M&M balls, fruits and vegetables and yellow pepper, respectively. The points at which the spectral signatures were extracted were marked by small circles in each image.

711 Table 1 Running times and peak signal to noise ratio (PSNR) of specularity removal method applied
712 for different hyperspectral and multispectral images acquired in different spectral ranges.

Image	**Image dimensions** $(\boldsymbol{m \times n \times \Omega})$	**Spectral range (nm)**	**Running time (S)**		**PSNR***	
			Shen and Cai's method	Proposed method	Shen and Cai's method	Proposed method
Fat	$850 \times 600 \times 300$	400-1000	0.61	2.48	76.88(71.02)	77.01(72.32)
Meat	$320 \times 650 \times 237$	900-1700	0.29	0.71	70.48(65.74)	71.33(66.66)
Ham	$900 \times 1650 \times 300$	400-1000	1.01	4.58	75.94(77.80)	76.90(78.57)
M&M	$640 \times 700 \times 80$	400-880	0.26	0.57	89.88(89.66)	85.14(84.99)
Mixed fruits	$1000 \times 900 \times 300$	400-1000	0.63	2.71	80.66(68.52)	82.41(69.96)
Pepper	$512 \times 512 \times 30$	400-700	0.34	1.08	83.02(73.78)	85.73(75.72)

713 * *Regional values of PSNR are written between two parentheses.*

714

715